

Unexpected Lack of Ferromagnetic Fluctuations Despite Ferromagnetic Substrate, with Commensurate Antiferromagnetic Fluctuations

Mohsen Shahbazi and Mohammad Ali Maleki

Department of Physics, Faculty of Science, University of Zanjan, University Blvd., 45371-38791, Zanjan, Iran

We investigate the presence of anti-ferromagnetic fluctuations in the longitudinal and transversal spin susceptibilities of a square lattice. The inclusion of both first and second neighbour hopping terms, along with exchange coupling, induces anti-ferromagnetic fluctuations over a finite range of fillings in both longitudinal and transversal static spin susceptibilities. The exchange field causes a splitting of the energy bands, resulting in two Van Hove singularities where the Fermi surface topology changes as the filling passes through these points. In the absence of on-site Hubbard interaction, we observe incommensurate anti-ferromagnetic fluctuations between the two Van Hove fillings. Beyond the second Van Hove singularity at $n = 1.03$, commensurate anti-ferromagnetic fluctuations dominate in both longitudinal and transversal spin susceptibilities. When incorporating a finite Hubbard interaction strength, U , we find that the commensurate anti-ferromagnetic fluctuations are preserved in both longitudinal and transversal dressed spin susceptibilities. However anti-ferromagnetic fluctuations vanish beyond a critical value of the Hubbard coupling strength, U_c . Despite the exchange field can be induced by a ferromagnetic substrate, we do not observe any ferromagnetic fluctuations in the system.

I. Introduction

The study of magnetic fluctuations in solid-state systems has garnered significant attention due to its fundamental importance and potential applications in spintronics and quantum computing [1, 2]. In particular, antiferromagnetic (AFM) fluctuations play a crucial role in understanding the magnetic properties and phase transitions in correlated electron systems [3, 4]. The interplay between electron interactions, lattice geometry, and external fields can lead to a rich variety of magnetic phenomena, making these systems a fertile ground for both theoretical and experimental research.

In square lattice systems, the inclusion of various hopping terms can influence the electronic structure and magnetic properties [5]. The combined effects of nearest-neighbor and next-nearest-neighbor hopping terms, along with an exchange field, can induce notable modifications in the band structure, leading to the emergence of Van Hove singularities in the density of states profile. Notice that the exchange field can be induced in the system by a ferromagnetic substrate [6, 7]. These singularities change the topology of the Fermi surfaces, thereby playing a crucial role in determining magnetic ordering and fluctuations [8, 9].

The magnetic ordering of a system is intricately influenced by the symmetries inherent in its Hamiltonian. In models of a square lattice system, involving first and second nearest neighbour hopping terms, the preservation of time reversal symmetry typically results in a paramagnetic state [10, 11]. However, the introduction of an exchange field breaks this crucial symmetry, leading to a variety of possible ordered spin states. Understanding these transitions is essential for comprehending the magnetic properties and potential applications of such systems in advanced technologies.

The nature and occurrence of ferromagnetic fluctua-

tions in the spin susceptibility for square lattice systems have been studied extensively [12, 13], particularly in models considering first and second nearest neighbour hopping terms within the Rashba-Hubbard framework [15, 16]. In this work, we investigate itinerant magnetic fluctuations in the presence of an exchange field. We calculate the bare (without Hubbard coupling) longitudinal and transverse susceptibilities in the first Brillouin zone and observe an absence of ferromagnetic fluctuations in the system. Instead, we find commensurate antiferromagnetic fluctuations at small electron fillings. Furthermore, we compute the dressed susceptibilities (with a finite Hubbard interaction coupling U), using the random phase approximation (RPA) [17]. The presence of the exchange field, coupled with the nearest and next-nearest neighbour hopping terms, significantly influences the magnetic properties of the system. Our findings indicate that commensurate antiferromagnetic fluctuations persist even with finite Hubbard interaction U , highlighting the robustness of this magnetic ordering in the presence of an exchange field.

II. Hamiltonian Modelling and Spin Susceptibility Characterization

framework, incorporating an exchange field term to accurately capture the system's electronic and magnetic properties. The precise modelling of the Hamiltonian is crucial for understanding the underlying physics of the material. The Hamiltonian for the square lattice structure, including the exchange field term, is formulated as follows

$$\hat{H} = -t \sum_{\langle i,j \rangle, \sigma} c_{i,\sigma}^\dagger c_{j,\sigma} - t' \sum_{\langle\langle i,j \rangle\rangle, \sigma} c_{i,\sigma}^\dagger c_{j,\sigma} - \mu \sum_{i,\sigma} c_{i,\sigma}^\dagger c_{i,\sigma} + \lambda_{ex} \sum_{i,\sigma} c_{i,\sigma}^\dagger \sigma_z c_{i,\sigma} \quad (1)$$

where, c_i^\dagger and c_i are the creation and annihilation operators. The Hamiltonian consists of four terms that represent different physical attributes within the system. The first term captures the nearest-neighbour hopping with a strength of t . The second term includes the next-nearest-neighbour hopping with a strength of t' , which provide a more comprehensive description of the electron dynamics. The third term stands for the chemical potential, which adjusts the electron density in the system and controls the overall energy level relative to the Fermi level. The final term represents the exchange field, characterized by an exchange strength of λ_{ex} , which can arise from the effect of a ferromagnetic substrate or other magnetic influences [6, 7]. Notice that σ_z , refers to the z component of Pauli matrix.

The electronic band structure of the system was analyzed for two sets of parameters: first with $t' = 0.3$ and $\lambda_{ex} = 0$, and second with $t' = 0.3$ and $\lambda_{ex} = 0.4$. Note that $t = 1$ was used in all calculations. Figure 1(a) illustrates the resulting band structures for these parameter sets. The introduction of the exchange field λ_{ex} causes a splitting of the energy bands for spin-up and spin-down electrons, leading to distinct density of states at the Fermi level for each spin orientation. The plot in Figure 1(a) illustrates the metallic phase of the system, highlighting key features such as the maximum at the K point and a saddle point at the M point of the first Brillouin zone (FBZ).

Additionally, the density of states (DOS) as a function of the filling factor was computed for the same sets of initial parameters. Figure 1(b) presents the DOS results, revealing significant details about the electronic states available at each energy level. In the absence of the exchange field ($\lambda_{ex} = 0$), there is a single Van Hove singularity at a filling factor $n_{vH} = 0.74$. This singularity corresponds to a peak in the DOS, indicating a high density of states at that energy level. When the exchange field is finite ($\lambda_{ex} = 0.4$), the DOS exhibits two Van Hove singularities, located at filling factors $n_{vH_1} = 0.52$ and $n_{vH_2} = 0.9$. These additional singularities are a direct consequence of the band splitting induced by the exchange field, reflecting the separate contributions of spin-up and spin-down electrons to the overall density of states. This behavior, as shown in Figure 1(b), underscores the significant impact of the exchange field on the electronic properties of the system, potentially leading to interesting magnetic phenomena.

So far, we have discussed the electronic properties of

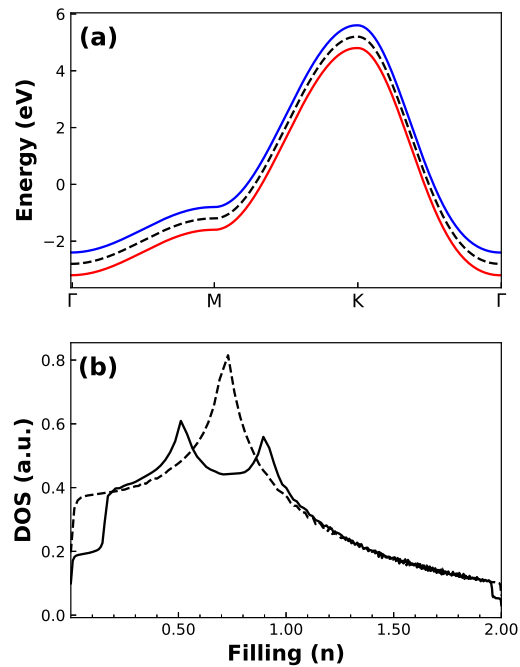


FIG. 1: (a) Electronic band structure of the system for two configurations: the dashed line represents the case with $t' = 0.3$ and $\lambda_{ex} = 0$; the solid lines represent the case with $t' = 0.3$ and $\lambda_{ex} = 0.4$. Red and blue lines represent the spin-up and spin-down states, respectively. (b) Density of states (DOS) as a function of filling (n), for the same two configurations: the dashed line corresponds to $t' = 0.3$ and $\lambda_{ex} = 0$; the solid line corresponds to $t' = 0.3$ and $\lambda_{ex} = 0.4$.

the system in the non-interacting limit. However, to gain a deeper understanding of the material's behaviour, it is crucial to consider the effects of electron-electron interactions, particularly the pair interaction of electron spins. In many materials, these interactions play a significant role in determining various physical properties, such as magnetism, superconductivity, and correlated electronic phases. The pair interaction of electron spins can be effectively described using the Hubbard model, which introduces an on-site interaction term to the Hamiltonian. This term accounts for the repulsive interaction between two electrons occupying the same lattice site, leading to significant modifications in the electronic structure and spin dynamics of the system. The Hamiltonian for the interacting system, incorporating the on-site Hubbard term, is given by

$$\hat{H}_{int} = U \sum_{\mathbf{k}, \mathbf{k}', \mathbf{q}} c_{\mathbf{k}\uparrow}^\dagger c_{\mathbf{k}+\mathbf{q}\uparrow} c_{\mathbf{k}'\downarrow}^\dagger c_{\mathbf{k}'-\mathbf{q}\downarrow} \quad (2)$$

where U represents the on-site Coulomb repulsion

strength, which penalizes double occupancy of electrons at the same site.

To thoroughly understand the magnetic properties of the system, it is crucial to analyse the magnetic response, which is characterized by the spin susceptibility. Spin susceptibility provides a quantitative measure of how the spin configuration of the system responds to an external magnetic field. This parameter is vital for understanding various magnetic phenomena, including magnetic ordering, spin waves, and critical behaviour near phase transitions. According to the basic definition, it can be written

$$\chi^{zz}(q, \tau) = \langle \mathbb{T} S^z(q, \tau) S^z(q, 0) \rangle \quad (3)$$

$$\chi^{+-}(q, \tau) = \langle \mathbb{T} S^+(q, \tau) S^-(q, 0) \rangle \quad (4)$$

where χ^{zz} and χ^{+-} refer to the longitudinal and transverse spin susceptibilities, respectively. τ stands for imaginary time, and \mathbb{T} denotes the time-ordering operator. By employing Wick's theorem[17], and performing a Fourier transformation with respect to time, one can express the spin susceptibilities as

$$\begin{aligned} \chi^{zz}(\mathbf{q}, i\omega_l) = & -\chi_{\uparrow\uparrow\uparrow\uparrow}(\mathbf{q}, i\omega_l) - \chi_{\downarrow\downarrow\downarrow\downarrow}(\mathbf{q}, i\omega_l) \\ & + \chi_{\uparrow\downarrow\downarrow\uparrow}(\mathbf{q}, i\omega_l) + \chi_{\downarrow\uparrow\uparrow\downarrow}(\mathbf{q}, i\omega_l) \end{aligned} \quad (5)$$

$$\chi^{+-}(\mathbf{q}, i\omega_l) = \chi_{\uparrow\downarrow\downarrow\uparrow}(\mathbf{q}, i\omega_l) + \chi_{\downarrow\uparrow\uparrow\downarrow}(\mathbf{q}, i\omega_l) \quad (6)$$

Here $\omega_l = 2l\pi/\beta$, represents the bosonic Matsubara frequency. Note that $\beta = \frac{1}{k_B T}$, where k_B is the Boltzmann constant and T is the temperature. More detailed calculations for longitudinal spin susceptibility are provided in Appendix A. The left-hand side terms of Equations 5 and 6 can be derived as follows

$$\begin{aligned} \chi_{\sigma_1\sigma_2\sigma_3\sigma_4}^{(0)}(\mathbf{q}, i\omega_l) = & \frac{-\hbar^2}{2N^2} \sum_{\mathbf{k}, ik_n} G_{\sigma_1\sigma_2}^{(0)}(\mathbf{k}, ik_n) \\ & G_{\sigma_3\sigma_4}^{(0)}(\mathbf{k} + \mathbf{q}, ik_n + i\omega_l) \end{aligned} \quad (7)$$

Here σ_i refers to spin-up or spin-down states. Due to the absence of spin-flip processes in our case, $G_{\uparrow\downarrow}^{(0)} = G_{\downarrow\uparrow}^{(0)} = 0$. Consequently, only the following bare Green's functions are finite

$$G_{\uparrow\uparrow}^{(0)}(ik_n, \mathbf{k}) = \frac{1}{ik_n - E_1(\mathbf{k})} \quad (8)$$

$$G_{\downarrow\downarrow}^{(0)}(ik_n, \mathbf{k}) = \frac{1}{ik_n - E_2(\mathbf{k})} \quad (9)$$

Here $k_n = (2n+1)\pi/\beta$ refers to the fermionic Matsubara frequency. $E_1(\mathbf{k})$ and $E_2(\mathbf{k})$ are the energy dispersions of the two bands. Consequently, there are only four finite bare spin susceptibilities, while the other possible states are zero. It should be noted that The spin susceptibility can be further decomposed into static ($\omega_l = 0$), and dynamic ($\omega_l \neq 0$) components, each revealing different aspects of the magnetic response.

III. Results of Bare and Dressed Spin Susceptibilities

To provide context, we first review certain characteristics of magnetic ordering of the system. In the square-lattice model with a finite value for first neighbour hopping of t , and without second neighbour hopping and exchange field ($t' = \lambda_{ex} = 0$), at half-filling (filling=1), the system behaves as a paramagnetic metal, where the spins are randomly oriented without an external magnetic field and align slightly with an applied magnetic field [18, 19]. The inclusion of the second-neighbour hopping term t' modifies the shape of the Fermi surface. It can either enhance or suppress certain nesting features depending on the sign and magnitude of t' . At half-filling, the original perfect nesting vector $Q = (\pi, \pi)$ for first-neighbour hopping is disrupted by the second-neighbor term [20]. This affects the tendency towards magnetic instabilities. Without interactions, the system remains a paramagnetic metal[21]. The modified band structure due to t' does not induce spontaneous magnetic ordering by itself. Consequently, the longitudinal and transverse spin susceptibilities are equal.

The system with finite values of first and second neighbour hopping, t and t' , preserve time reversal symmetry and possesses spin rotational symmetry group of $SU(2)$. The introduction of finite values of exchange field, $\lambda_{ex} \neq 0$, breaks the full $SU(2)$ spin rotational symmetry down to $U(1)$, as it selects a preferred direction for the spins. Moreover, the exchange field breaks time-reversal symmetry because reversing time flips the spin direction, which is not energetically favourable in the presence of the exchange field [22]. Furthermore, the system's magnetic susceptibility change with the exchange field, so that the longitudinal and transverse spin susceptibilities are not equal, any more.

The phase diagrams of the system for the static longitudinal spin susceptibility at (π, π) are calculated over ranges of t', λ_{ex} and n (see Figures 2(a) and 2(b)). These diagrams reveal that the longitudinal spin susceptibility exhibits large values near half-filling ($n = 1$), particularly within the parameter $0 \leq t' \leq 0.4$ and $0 \leq \lambda_{ex} \leq 0.4$. As the electron filling moves further away from $n = 1$, the value of the longitudinal spin susceptibility decreases. This behaviour indicates the possibility of presence of

the commensurate anti-ferromagnetic fluctuations within these specific ranges of parameters, highlighting the potential for anti-ferromagnetic ordering in the system. Notably, phase diagrams of the system for the static longitudinal spin susceptibility at $(0,0)$ over the same parameter ranges show zero values for the longitudinal susceptibility across almost the entire range (not shown). This indicates the possible absence of spin fluctuations at $(0,0)$, leading to the interesting conclusion that there are no ferromagnetic fluctuations in the system, even in the presence of a ferromagnetic substrate.

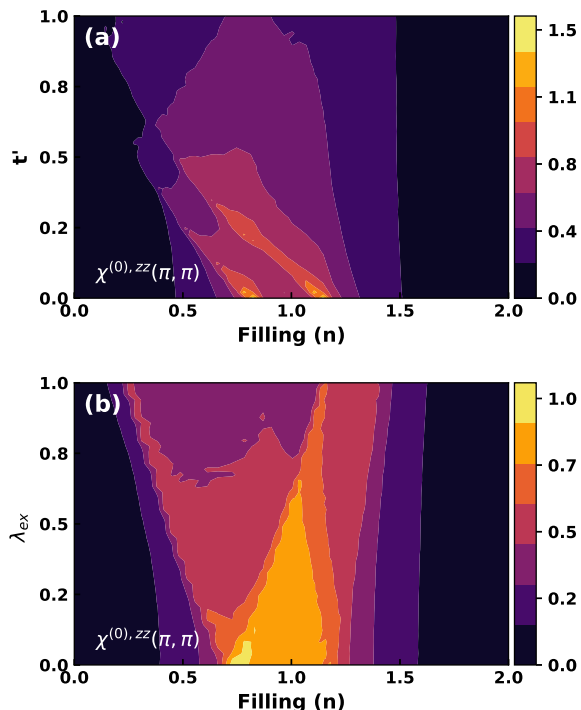


FIG. 2: Phase diagrams of the bare longitudinal static spin susceptibility at the (π, π) point for two different states. Panel(a) the phase diagram as a function of next-nearest neighbour hopping t' and filling; while panel (b) presents the phase diagram as a function of the exchange field λ_{ex} and filling. All calculations were performed at a finite temperature of $T = 0.01$

Another factor that can significantly impact spin susceptibility is the topology of the Fermi surface [10, 14]. It is important to note that when the Fermi surface is centered around the Γ point, it becomes hole-like. Conversely, if it is centered around (π, π) in the first Brillouin zone, it becomes electron-like. Figure 3 illustrates the Fermi surfaces of the system under the initial conditions: $t = 1, t' = 0.3$ and $\lambda_{ex} = 0.4$, for different electron fillings. For $n = 0.43$ both Fermi surfaces for opposite spins are electron-like as shown in the Figure 3(a). This indicates a

predominance of electron-like carriers at this filling. Figures 3(b) and 3(c) display the Fermi surfaces for $n = 0.62$ and $n = 0.78$, respectively, which lie between two Van Hove singularities. At these fillings, the system exhibits a mixed topology: one Fermi surface is electron-like, and the other is hole-like. This indicates the presence of both types of carriers, contributing to the complexity of the system's electronic structure and spin dynamics. As the filling increases beyond n_{vH_2} , the topology of the Fermi surface undergoes another transition. In this situation, both Fermi surfaces become hole-like, as illustrated in Figure 3(d). This indicates that hole-like carriers are dominant at this filling.

Next, we calculate the static bare spin susceptibilities for the same initial conditions used to obtain the Fermi surfaces, as shown in Figure 4. Before examining Figure 4, it is important to explain how magnetic fluctuations can be inferred from spin susceptibility plots. By analysing the peaks in the spin susceptibility, we can identify various magnetic behaviors: ferromagnetic tendencies are characterized by a peak at $\mathbf{q} = (0,0)$; commensurate anti-ferromagnetic behaviour is evidenced by a peak at $\mathbf{q} = (\pi, \pi)$; and incommensurate anti-ferromagnetic behaviour is represented by a peak at $\tilde{\mathbf{q}}$, which typically resides close to, but not exactly at $\mathbf{q} = (\pi, \pi)$. Figure 4(c) demonstrates incommensurate anti-ferromagnetic fluctuations via the longitudinal spin susceptibility at $n = 0.78$. For a small electron filling, $n = 1.03$, the longitudinal spin susceptibility shows commensurate anti-ferromagnetic fluctuations, as illustrated in Figure 4(d). These figures highlight how the nature of the magnetic fluctuations evolves with changing electron filling. Furthermore, the transverse spin susceptibilities for fillings of $n = 0.62$ and $n = 0.78$ reveal incommensurate anti-ferromagnetic fluctuations, as illustrated in Figures 4(f) and 4(g). These figures show distinct peaks at wave vectors $\tilde{\mathbf{q}}$, which are close to but not exactly at $\mathbf{q} = (\pi, \pi)$, indicating that the system exhibits complex spin ordering rather than simple commensurate anti-ferromagnetic order. This behavior highlights the sensitivity of the transverse spin susceptibility to variations in electron filling and its role in capturing subtle changes in the magnetic structure. In contrast, the transverse spin susceptibility at $n = 1.03$ demonstrates commensurate antiferromagnetic fluctuations, as depicted in Figure 4(h). Here, a prominent peak at $\mathbf{q} = (\pi, \pi)$ is observed, signifying a well-defined antiferromagnetic order with a modulation vector aligned with the lattice periodicity. This consistency between longitudinal and transverse susceptibilities at $n = 1.03$ underscores the robust nature of commensurate antiferromagnetic ordering at this specific filling.

So far, we have focused on the bare spin susceptibilities $\chi^{(0)}(\mathbf{q})$, which provide insight into the intrinsic magnetic properties of the system without considering spin interactions of pairs. However, to achieve a more accurate and comprehensive understanding of the

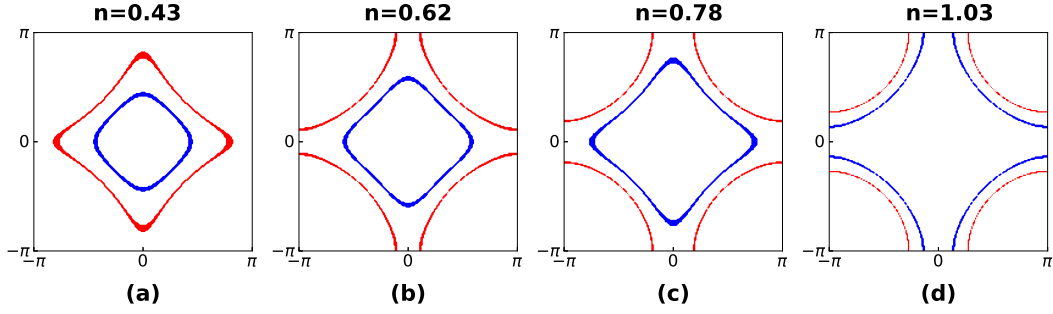


FIG. 3: Fermi surfaces of the system with $t' = 0.3$, $\lambda_{ex} = 0.4$ and different fillings. Panel (a) represents the Fermi surface with a filling less than n_{vH_1} . Panels (b) and (c) show the Fermi surfaces with fillings between the two singularities, n_{vH_1} and n_{vH_2} . Panel (d) illustrates the Fermi surface with a filling greater than n_{vH_2} .

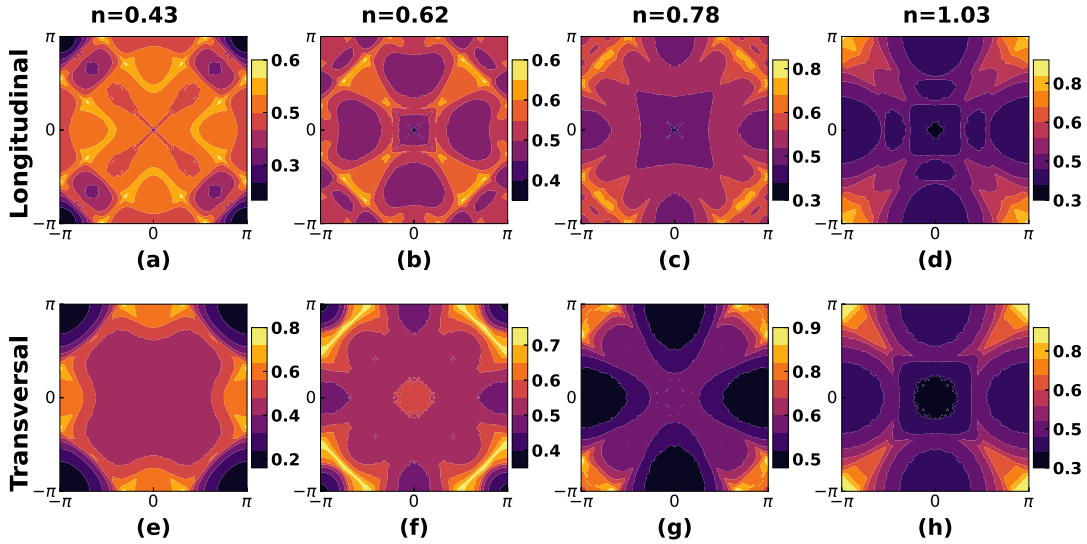


FIG. 4: Bare static spin susceptibilities with $t' = 0.3$, $\lambda_{ex} = 0.4$ and four different fillings. Panels (a-d) represent the longitudinal bare susceptibilities corresponding to the same fillings as the Fermi surface plots. Panels (e-h) illustrate the transverse bare susceptibilities for the same filling levels as in the Fermi surface plots.

system's magnetic behaviour, it is essential to take into account the effects of interactions. As previously mentioned, we incorporate the on-site Hubbard term to account for the electron-electron interactions within the system. These interaction can significantly modify the spin susceptibilities, leading to what are known as dressed spin susceptibilities $\chi(\mathbf{q})$. To investigate the impact of this interaction, we employ the random phase approximation (RPA)[17], a powerful method that allows us to incorporate the interaction systematically. The RPA provides a framework to account for the collective effects of spin fluctuations, enhancing our understanding of the magnetic response of the system. In the following, we present the six non-zero components of the dressed spin susceptibilities obtained through the RPA, highlighting the changes brought about by the

inclusion of on-site Coulomb repulsion:

$$\chi_{\uparrow\uparrow\uparrow\uparrow}^{RPA} = \frac{\chi_{\uparrow\uparrow\uparrow\uparrow}^{(0)}}{1 - U^2 \chi_{\uparrow\uparrow\uparrow\uparrow}^{(0)} \chi_{\downarrow\downarrow\downarrow\downarrow}^{(0)}} \quad (10)$$

$$\chi_{\downarrow\downarrow\downarrow\downarrow}^{RPA} = \frac{\chi_{\downarrow\downarrow\downarrow\downarrow}^{(0)}}{1 - U^2 \chi_{\downarrow\downarrow\downarrow\downarrow}^{(0)} \chi_{\uparrow\uparrow\uparrow\uparrow}^{(0)}} \quad (11)$$

$$\chi_{\uparrow\downarrow\uparrow\downarrow}^{RPA} = \frac{U \chi_{\downarrow\downarrow\downarrow\downarrow}^{(0)} \chi_{\uparrow\uparrow\uparrow\uparrow}^{(0)}}{1 - U^2 \chi_{\downarrow\downarrow\downarrow\downarrow}^{(0)} \chi_{\uparrow\uparrow\uparrow\uparrow}^{(0)}} \quad (12)$$

IV. Conclusion

In summary, we have investigated the occurrence of the anti-ferromagnetic fluctuations in a system described by a Hamiltonian that includes first and second nearest neighbor hopping terms, an exchange field, and an on-site Hubbard term on a square lattice. The exchange field induces a band splitting, leading to two Van Hove singularities. In the absence of the Hubbard interaction, we find that incommensurate anti-ferromagnetic fluctuations dominate in the bare longitudinal and transversal spin susceptibilities, for fillings between the two Van Hove singularities. For fillings, $n = 1.03$, greater than the larger Van Hove filling, commensurate anti-ferromagnetic fluctuations become prevalent. With the inclusion of the Hubbard term, the dressed longitudinal and transversal susceptibilities reveal that commensurate anti-ferromagnetic fluctuations are preserved at the same filling of $n = 1.03$. This indicates that the commensurate anti-ferromagnetic fluctuation is robust at this specific electron filling. However, anti-ferromagnetic fluctuations vanish beyond a critical Hubbard coupling strength of $U_c \simeq 2.5$. Although a ferromagnetic substrate can induce an exchange field, we do not observe any ferromagnetic fluctuations in the system. Our findings underscore the critical role of electron interactions in shaping the magnetic properties of the system. They provide valuable insights into the stability and persistence of commensurate anti-ferromagnetic fluctuations at specific small electron fillings, particularly in the presence of varying the strengths on-site Coulomb repulsion.

A. Derivations of the longitudinal spin susceptibilities

In the context of condensed matter physics, the longitudinal spin susceptibility $\chi^{zz}(q, \tau)$, is a fundamental quantity that characterizes the response of a spin system to an external perturbation aligned with the direction of the spin. Mathematically, the longitudinal spin susceptibility is defined as

$$\chi^{zz}(\mathbf{q}, \tau) = \langle T S^z(\mathbf{q}, \tau) S^z(-\mathbf{q}, 0) \rangle \quad (\text{A1})$$

where, τ refers to imaginary time operator. According to the definition of the z-component of the spin operator, we have

$$S^z(\mathbf{q}, \tau) = \frac{\hbar}{2N^2} \sum_{\mu, k} e^{-i\mathbf{q}\cdot\boldsymbol{\mu}} \left[c_{k,\uparrow}^\dagger(\tau) c_{k+\mathbf{q},\uparrow}(\tau) - c_{k,\downarrow}^\dagger(\tau) c_{k+\mathbf{q},\downarrow}(\tau) \right] \quad (\text{A2})$$

By substituting Equation of A1 into Equation A2, we obtain

$$\chi_{\uparrow\downarrow\uparrow}^{RPA} = \frac{U \chi_{\downarrow\downarrow\downarrow}^{(0)} \chi_{\uparrow\uparrow\uparrow}^{(0)}}{1 - U^2 \chi_{\downarrow\downarrow\downarrow}^{(0)} \chi_{\uparrow\uparrow\uparrow}^{(0)}} \quad (\text{13})$$

$$\chi_{\uparrow\uparrow\downarrow}^{RPA} = \frac{\chi_{\uparrow\uparrow\downarrow}^{(0)}}{1 - U \chi_{\uparrow\uparrow\downarrow}^{(0)}} \quad (\text{14})$$

$$\chi_{\downarrow\downarrow\uparrow}^{RPA} = \frac{\chi_{\downarrow\downarrow\uparrow}^{(0)}}{1 - U \chi_{\downarrow\downarrow\uparrow}^{(0)}} \quad (\text{15})$$

Further details on the calculation of the non-zero elements of the dressed spin susceptibilities are provided in Appendix B.

Figure 5 illustrates the longitudinal dressed spin susceptibilities for various interaction strengths U , at a filling of $n = 1.03$. As observed from Figure 5, the static dressed susceptibility maintains a pronounced peak at (π, π) , indicating that the commensurate antiferromagnetic fluctuation is preserved despite the inclusion of interaction effects. This persistent peak suggests that the system remains robustly in a commensurate anti-ferromagnetic state even as the interaction strength U is varied. The preservation of the peak at (π, π) , underscores the stability of the antiferromagnetic order under the influence of electron-electron interactions. Note that this pronounced peak at (π, π) disappears at the critical point $U_c \simeq 2.5$. It highlights the dominant role of commensurate antiferromagnetic fluctuations in the magnetic response of the system at this particular filling. This finding is significant as it demonstrates that the essential magnetic characteristics are not only intrinsic to the bare system but also resilient to the perturbations introduced by the Hubbard interaction.

Figure 6, presents the transversal dressed spin susceptibilities for various strengths of the Hubbard interaction U at small electron filling, $n = 1.03$. The static transversal susceptibility exhibits a pronounced peak at (π, π) across different interaction strengths, indicating robust commensurate anti-ferromagnetic order. It is important to note that the pronounced peak at (π, π) vanishes at the critical point $U_c \simeq 2.5$. Analyzing the dressed transversal spin susceptibilities provides a comprehensive view of the system's magnetic response. The consistency between the longitudinal and transversal susceptibilities suggests that the underlying magnetic order is intrinsically commensurate and stable in small electron filling $n = 1.03$. This robustness could have significant implications for the understanding and potential manipulation of magnetic phases in correlated electron systems, offering insights into how these systems maintain their magnetic properties even in the presence of strong interactions.

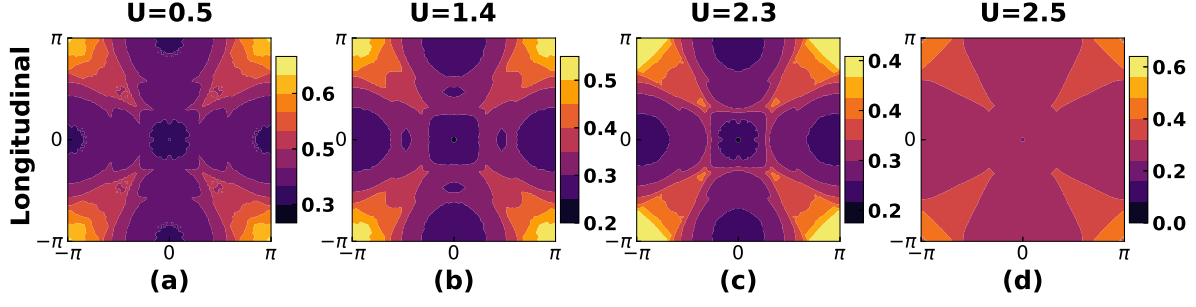


FIG. 5: Static longitudinal dressed spin susceptibilities at $n = 1.03$ for different values of the on-site Hubbard coupling.

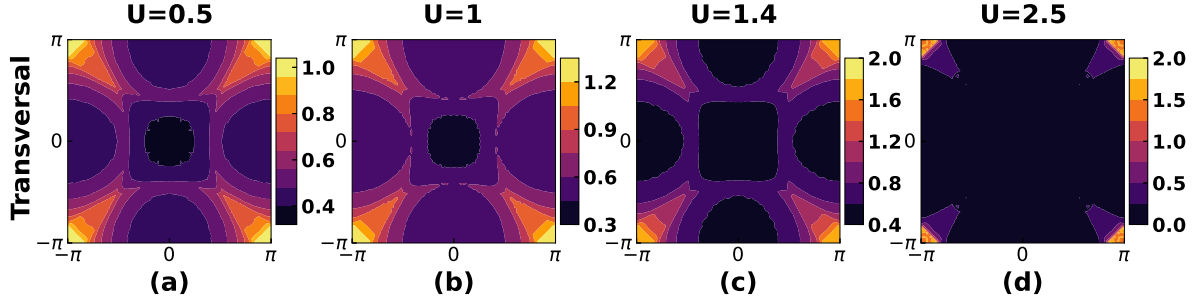


FIG. 6: Static transversal dressed spin susceptibilities at $n = 1.03$ for different values of the on-site Hubbard coupling.

$$\begin{aligned}
 \chi^{zz}(\mathbf{q}, \tau) = & \\
 & - \frac{\hbar}{2N^2} \sum_{k, k'} [\langle \mathbb{T} c_{k, \uparrow}^\dagger(\tau) c_{k+\mathbf{q}, \uparrow}^\dagger(\tau) c_{k'', \uparrow}(0) c_{k''-\mathbf{q}, \uparrow}(0) \rangle \\
 & - \langle \mathbb{T} c_{k, \uparrow}^\dagger(\tau) c_{k+\mathbf{q}, \uparrow}^\dagger(\tau) c_{k'', \downarrow}(0) c_{k''-\mathbf{q}, \downarrow}(0) \rangle \\
 & - \langle \mathbb{T} c_{k, \downarrow}^\dagger(\tau) c_{k+\mathbf{q}, \downarrow}^\dagger(\tau) c_{k'', \uparrow}(0) c_{k''-\mathbf{q}, \uparrow}(0) \rangle \\
 & - \langle \mathbb{T} c_{k, \downarrow}^\dagger(\tau) c_{k+\mathbf{q}, \downarrow}^\dagger(\tau) c_{k'', \downarrow}(0) c_{k''-\mathbf{q}, \downarrow}(0) \rangle] \quad (\text{A3})
 \end{aligned}$$

Then, applying Wick's theorem, we can write

$$\begin{aligned}
 \chi^{zz}(\mathbf{q}, \tau) = & - \frac{\hbar}{2N^2} \sum_{k, k'} \\
 & [- \langle \mathbb{T} c_{k+\mathbf{q}, \uparrow}(\tau) c_{k'', \uparrow}^\dagger(0) \rangle \langle \mathbb{T} c_{k''-\mathbf{q}, \uparrow}(0) c_{k, \uparrow}^\dagger(\tau) \rangle \\
 & + \langle \mathbb{T} c_{k+\mathbf{q}, \uparrow}(\tau) c_{k'', \downarrow}^\dagger(0) \rangle \langle \mathbb{T} c_{k''-\mathbf{q}, \downarrow}(0) c_{k, \uparrow}^\dagger(\tau) \rangle \\
 & + \langle \mathbb{T} c_{k+\mathbf{q}, \downarrow}(\tau) c_{k'', \uparrow}^\dagger(0) \rangle \langle \mathbb{T} c_{k''-\mathbf{q}, \uparrow}(0) c_{k, \downarrow}^\dagger(\tau) \rangle \\
 & - \langle \mathbb{T} c_{k+\mathbf{q}, \downarrow}(\tau) c_{k'', \downarrow}^\dagger(0) \rangle \langle \mathbb{T} c_{k''-\mathbf{q}, \downarrow}(0) c_{k, \downarrow}^\dagger(\tau) \rangle] \quad (\text{A4})
 \end{aligned}$$

Then it can be expressed as

$$\begin{aligned}
 \chi^{zz}(\mathbf{q}, \tau) = & - \frac{\hbar}{2N^2} \sum_{k, k'} \\
 & [- G_{\uparrow\uparrow}(k+\mathbf{q}, \tau) G_{\uparrow\uparrow}(k, -\tau) + G_{\uparrow\downarrow}(k+\mathbf{q}, \tau) G_{\downarrow\uparrow}(k, -\tau) \\
 & + G_{\downarrow\uparrow}(k+\mathbf{q}, \tau) G_{\uparrow\downarrow}(k, -\tau) - G_{\downarrow\downarrow}(k+\mathbf{q}, \tau) G_{\downarrow\downarrow}(k, -\tau)] \quad (\text{A5})
 \end{aligned}$$

Therefore, by performing a Fourier transformation with respect to time, one can express

$$\begin{aligned} \chi^{zz}(\mathbf{q}, i\omega_l) = & -\chi_{\uparrow\uparrow\uparrow\uparrow}(\mathbf{q}, i\omega_l) - \chi_{\downarrow\downarrow\downarrow\downarrow}(\mathbf{q}, i\omega_l) \\ & + \chi_{\uparrow\downarrow\downarrow\uparrow}(\mathbf{q}, i\omega_l) + \chi_{\downarrow\uparrow\uparrow\downarrow}(\mathbf{q}, i\omega_l) \end{aligned} \quad (\text{A6})$$

The same procedure can be applied to obtain the transversal spin susceptibility.

B. Derivation of one of the RPA spin susceptibility elements

There are sixteen possible components for spin susceptibility in total, but in our system, only six of these components are non-zero due to the absence of spin-flip processes. In this section, we explain the calculation of one of the non-zero components of dressed spin susceptibility, $\chi_{\uparrow\uparrow\uparrow\uparrow}^{RPA}$, as an example. The expansion of this component is:

$$\begin{aligned} \chi_{\uparrow\uparrow\uparrow\uparrow}^{RPA} = & \chi_{\uparrow\uparrow\uparrow\uparrow}^{(0)} + \chi_{\uparrow\uparrow\uparrow\uparrow}^{(0)} U \chi_{\uparrow\uparrow\uparrow\uparrow}^{(0)} U \chi_{\uparrow\uparrow\uparrow\uparrow}^{(0)} \\ & + \chi_{\uparrow\uparrow\uparrow\uparrow}^{(0)} U \chi_{\uparrow\uparrow\uparrow\uparrow}^{(0)} U \chi_{\uparrow\uparrow\uparrow\uparrow}^{(0)} U \chi_{\uparrow\uparrow\uparrow\uparrow}^{(0)} U \chi_{\uparrow\uparrow\uparrow\uparrow}^{(0)} \\ & + \dots \end{aligned} \quad (\text{B1})$$

In the context of Feynman diagrams, spin susceptibilities are represented by specific diagrammatic elements: bubbles and ladders. These diagrams help visualize and calculate the modifications to the susceptibilities due to interactions. The corresponding RPA expansion of $\chi_{\uparrow\uparrow\uparrow\uparrow}^{RPA}$ is shown in the Figure 7

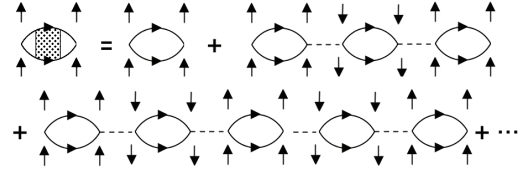


FIG. 7: A detailed schematic of the diagrammatic expansion for $\chi_{\uparrow\uparrow\uparrow\uparrow}^{RPA}$. Solid lines with arrows illustrate propagators. The spin orientations are shown by arrows out of bubbles. Dashed lines indicate the interaction term U

By factoring, we arrive at the diagram shown in Figure 8

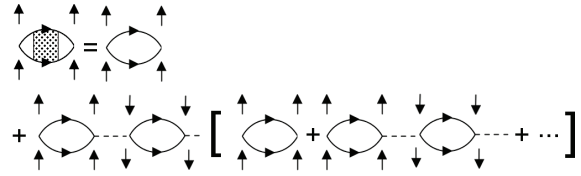


FIG. 8: Factoring of the expansion of the $\chi_{\uparrow\uparrow\uparrow\uparrow}^{RPA}$

After renormalization, the result can be seen in Figure 9

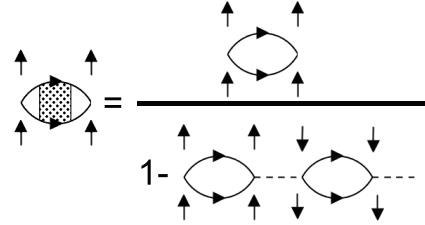


FIG. 9: Schematic representation of the Feynman diagram for the derived $\chi_{\uparrow\uparrow\uparrow\uparrow}^{RPA}$

Which one can write as the corresponding formula as

$$\chi_{\uparrow\uparrow\uparrow\uparrow}^{RPA} = \frac{\chi_{\uparrow\uparrow\uparrow\uparrow}^{(0)}}{1 - U^2 \chi_{\uparrow\uparrow\uparrow\uparrow}^{(0)} \chi_{\downarrow\downarrow\downarrow\downarrow}^{(0)}} \quad (\text{B2})$$

The rest of the non-zero components of dressed spin susceptibilities can be obtained using a similar procedure.

References

[1] Žutić, I., Fabian, J., & Sarma, S. D. (2004). Spintron-

ics: Fundamentals and applications. *Reviews of Modern*

- Physics*, 76(2), 323.
- [2] Awschalom, D. D., Bassett, L. C., Dzurak, A. S., Hu, E. L., & Petta, J. R. (2013). Quantum spintronics: engineering and manipulating atom-like spins in semiconductors. *Science*, 339(6124), 1174–1179.
- [3] Dagotto, E. (1994). Correlated electrons in high-temperature superconductors. *Reviews of Modern Physics*, 66(3), 763.
- [4] Scalapino, D. J. (2012). A common thread: The pairing interaction for unconventional superconductors. *Reviews of Modern Physics*, 84(4), 1383.
- [5] Lee, P. A., Nagaosa, N., & Wen, X.-G. (2006). Doping a Mott insulator: Physics of high-temperature superconductivity. *Reviews of Modern Physics*, 78(1), 17.
- [6] Zhao, C., Norden, T., Zhang, P., Zhao, P., Cheng, Y., Sun, F., Parry, J. P., Taheri, P., Wang, J., Yang, Y., et al. (2017). Enhanced valley splitting in monolayer WSe₂ due to magnetic exchange field. *Nature Nanotechnology*, 12(8), 757–762.
- [7] Shahbazi, M. (2018). Linear giant Stark effect in WSe₂ nanoribbons. *Physica B: Condensed Matter*, 545, 159–166.
- [8] Graser, S., Maier, T. A., Hirschfeld, P. J., & Scalapino, D. J. (2009). Near-degeneracy of several pairing channels in multiorbital models for the Fe pnictides. *New Journal of Physics*, 11(2), 025016.
- [9] O. Vafek and A. Vishwanath, *Dirac fermions in solids: from high- T_c cuprates and graphene to topological insulators and Weyl semimetals*, *Annu. Rev. Condens. Matter Phys.* **5**, 83–112 (2014).
- [10] Rømer, A. T., Kreisel, A., Eremin, I., Malakhov, M. A., Maier, T. A., Hirschfeld, P. J., & Andersen, B. M. (2015). Pairing symmetry of the one-band Hubbard model in the paramagnetic weak-coupling limit: A numerical RPA study. *Physical Review B*, 92(10), 104505.
- [11] Rømer, A. T., Maier, T. A., Kreisel, A., Eremin, I., Hirschfeld, P. J., & Andersen, B. M. (2020). Pairing in the two-dimensional Hubbard model from weak to strong coupling. *Physical Review Research*, 2(1), 013108.
- [12] Šimković IV, F., Liu, X.-W., Deng, Y., & Kozik, E. (2016). Ground-state phase diagram of the repulsive fermionic t - t' Hubbard model on the square lattice from weak coupling. *Physical Review B*, 94(8), 085106.
- [13] Zheng, B.-X., & Chan, G. K.-L. (2016). Ground-state phase diagram of the square lattice Hubbard model from density matrix embedding theory. *Physical Review B*, 93(3), 035126.
- [14] Hlubina, R. (1999). Phase diagram of the weak-coupling two-dimensional t - t' Hubbard model at low and intermediate electron density. *Physical Review B*, 59(14), 9600.
- [15] A. Greco and A. P. Schnyder, *Mechanism for unconventional superconductivity in the hole-doped Rashba-Hubbard model*, *Physical Review Letters* **120**, 177002 (2018).
- [16] A. Greco, M. Bejas, and A. P. Schnyder, *Ferromagnetic fluctuations in the Rashba-Hubbard model*, *Physical Review B* **101**, 174420 (2020).
- [17] H. Bruus and K. Flensberg, *Many-body quantum theory in condensed matter physics: an introduction* (OUP Oxford, 2004).
- [18] N. Furukawa and M. Imada, *Metal-insulator transition in the two-dimensional Hubbard model*, *Physica B: Condensed Matter* **186**, 931–934 (1993).
- [19] M.-H. Zeng, T. Ma, and Y.-J. Wang, *Phase diagram of the Hubbard model on a square lattice: A cluster slave-spin study*, *Physical Review B* **104**, 094524 (2021).
- [20] M. D. Johannes and I. I. Mazin, *Fermi surface nesting and the origin of charge density waves in metals*, *Physical Review B* **77**, 165135 (2008).
- [21] H. Q. Lin and J. E. Hirsch, *Two-dimensional Hubbard model with nearest-and next-nearest-neighbor hopping*, *Physical Review B* **35**, 3359 (1987).
- [22] P. Liu, J. Li, J. Han, X. Wan, and Q. Liu, *Spin-group symmetry in magnetic materials with negligible spin-orbit coupling*, *Physical Review X* **12**, 021016 (2022).